Battery Energy

WILEY

RESEARCH ARTICLE OPEN ACCESS

Intraparticular Heterogeneity Limits Capacity in Lithium–Sulfur Batteries With Carbonate Electrolyte

Ayca Senol Gungor[1] | Jean-Marc von Mentlen[1] | Francisco Javier García-Soriano[2] | Christian Zaubitzer[3] | Milivoj Plodinec[3] | Jean G. A. Ruthes[4] | Sven Dunkel[5] | Volker Presser[4,6,7] | Alen Vizintin[2] | Vanessa Wood[1] | Christian Prehal[5]

[1]Department of Information Technology and Electrical Engineering, ETH Zürich, Zürich, Switzerland | [2]Department of Materials Chemistry, National Institute of Chemistry, Ljubljana, Slovenia | [3]Scientific Center for Optical and Electron Microscopy, ScopeM, ETH Zürich, Zürich, Switzerland | [4]INM - Leibniz Institute for New Materials, Saarbrücken, Germany | [5]Department of Chemistry and Physics of Materials, University of Salzburg, Salzburg, Austria | [6]Department of Materials Science and Engineering, Saarland University, Saarbrücken, Germany | [7]saarene – Saarland Center for Energy Materials and Sustainability, Saarbrücken, Germany

Correspondence: Vanessa Wood (vwood@ethz.ch) | Christian Prehal (christian.prehal@plus.ac.at)

Received: 9 December 2025 | **Revised:** 25 February 2026 | **Accepted:** 16 March 2026

Funding: European Research Council, Grant/Award Number: 101078271; Horizon 2020 Framework Programme, Grant/Award Number: 958174

Keywords: carbon particle size | CEI formation | cryogenic electron microscopy | electrochemical performance | intraparticular heterogeneity | lithium–sulfur batteries | nanoporous carbons | solid-state sulfur conversion

ABSTRACT

The formation of a stable cathode-electrolyte interphase (CEI) is critical for the performance of lithium–sulfur (Li–S) batteries with carbonate-based electrolytes, as it suppresses parasitic polysulfide reactions and enables solid-state sulfur conversion. In nanoporous carbon hosts, the CEI together with nanopore confinement plays a key role in capacity retention and long-term cycling. Yet, its spatial formation, stability, and contribution to electrochemical performance remain poorly understood, partly due to challenges in characterization caused by beam and air sensitivity. Here, we employ cryogenic transmission electron microscopy (cryo-TEM) with electron energy loss spectroscopy and energy-dispersive X-ray spectroscopy, X-ray photoelectron spectroscopy and electrochemical testing together with galvanostatic intermittent titration technique measurements to elucidate how carbon particle size affects CEI formation and electrochemical performance. We find that the CEI is not a uniform surface film but extends heterogeneously into the particle bulk. Mass transport during the first discharge dictates CEI development, and larger particles suffer from inactive regions due to the preferential CEI formation only in the outer regions of the particles. During extended cycling, charge transfer resistance at confined CEI/active material/carbon interfaces emerges as the dominant performance-limiting factor. These findings show that particle size controls CEI formation during initial discharge, offering guidance for designing carbon hosts from nano- to micrometer length scales in Li–S battery cathodes.

1 | Introduction

Lithium–sulfur (Li–S) batteries containing carbonate electrolyte offer several advantages over ether-based electrolytes, including compatibility with lean electrolyte conditions and therefore higher energy densities [1, 2], lower flammability [3], and significant mitigation of capacity fading associated with soluble polysulfides [4, 5]. The conversion between sulfur and Li_2S can proceed via a solid-state pathway in carbonate electrolytes, enabled by the in-situ formation of a protective cathode-electrolyte interphase (CEI) [1, 2, 6, 7] and supported by the physical confinement in carbon micropores (pore size below 2 nm) [8–13]. This interphase formation is driven by the electrochemical decomposition of the electrolyte and a nucleophilic

reaction between the carbonate molecules and polysulfides during the first discharge [14–19].

The CEI comprises a complex structure containing LiF, Li_2CO_3, lithium alkyl carbonate ($ROCO_2Li$)/lithium alkyl oxides (ROLi), polycarbonates, thiocarbonates, and sulfur-oxygen species, such as Li_xSO_y (e.g., Li_2SO_4) [1, 6, 7, 11, 18, 20–22]. Its formation is essential for suppressing polysulfide side reactions [4, 22], minimizing the accumulation of poorly conductive discharge products on the cathode surface, and enabling stable cycling performance in contrast to ether-based electrolytes [6, 10, 18, 21].

Previous studies on sulfur–carbon composites generally report a homogeneous sulfur distribution on a particle scale after melt infiltration, as evidenced by electron microscopy with conventional energy dispersive X-ray spectroscopy (EDS) analyses, and thus focus primarily on cathode preparation quality [23–27]. However, such measurements provide limited insight into heterogeneity that may develop during electrochemical operation, particularly during the first discharge when CEI formation and solid-state sulfur conversion occur. In carbonate-based systems relying on physical confinement, this discharge-induced heterogeneity is expected to play a decisive role in governing electrochemical performance [28, 29]. Despite this importance, the structure and formation dynamics of the CEI in nanoporous carbons remain poorly understood [10, 16]. Surface-sensitive techniques such as XPS have identified CEI components on the particle surface [1, 6, 20–22]. In contrast, bulk-sensitive probes like nuclear magnetic resonance [11, 30], Fourier transform infrared spectroscopy [19, 31], or X-ray methods like X-ray absorption spectroscopy and X-ray diffraction (XRD) [17] have provided complementary bulk chemical information. However, these approaches either lack spatial resolution or depth sensitivity [32], limiting insights into where and how the CEI forms inside carbon nanoparticles. Raman spectroscopy could, in principle, provide spatial mapping, but the assignment of peaks requires complex theoretical modeling [23]. Overall, a clear link between the CEI structure and electrochemical performance has yet to be established, particularly within the confined geometry of high-surface-area nanoporous carbons where electrolyte access may be restricted.

To bridge this gap, electron microscopy combined with spectroscopy offers a powerful approach. Techniques such as scanning transmission electron microscopy (STEM) with EDS or electron energy loss spectroscopy (EELS) provide spatially resolved chemical information at the nanometer scale [33, 34] and have been successfully applied to study the CEI [35, 36] and SEI [37–42], both in Li–S batteries and other types of batteries. However, their application to Li–S batteries is complicated [32] by the air, beam, and vacuum sensitivity of sulfides, sulfur, and interphase components [16, 43–48]. Cryogenic electron microscopy [49], including cryo-FIB-SEM for lamella preparation [32, 43] and cryo-STEM/EELS, enables the preservation of the native chemical environment and offers high-resolution structural and compositional mapping across individual particles.

In this study, we investigate the spatially resolved CEI formation, its relationship to the nano- and microscale structure of the commercially available C/S composite cathode without further modification, and its correlation with electrochemical performance in carbonate-based Li-S batteries. Building on our previous work, which focused on design parameters such as nanopore size and sulfur loading [28], this study highlights the interplay between microstructure (particle-level) and nanostructure (pore-level) in governing the overall electrochemical behavior. Nanoporous carbons with identical average pore size (0.8 nm) but different particle sizes spanning from 1 to 8 μm are tested by means of galvanostatic cycling and the galvanostatic intermittent titration technique (GITT). Cryo-FIB-SEM and cryo-STEM/EELS reveal the internal heterogeneity of CEI and active material distribution in a single discharged C/S particle. Cryo-TEM analysis and X-ray photoelectron spectroscopy (XPS) of discharged Li–S battery electrodes further highlight the complex CEI structure on the particle surface. A simple analysis that considers the particle-size-dependent intraparticular heterogeneity rationalizes the correlation between active volume fraction, particle size, and capacity.

2 | Results and Discussion

We start by investigating the effect of the conductive nanoporous carbon microstructure on specific capacity and rate performance (Figure 1). To minimize the influence of variables other than particle size, the same activated carbon material was used throughout the study. The as-received activated carbon, with a pore size of 0.8 nm [28], is denoted as AC08 and has an average particle size of 8–9 μm with a broad size distribution (Figure 1a). Particle downsizing was achieved through ball milling, with the milling rate controlling the resulting particle size. Ball milling at 500 rpm and 800 rpm for 2h reduced the average particle size to 4–5 μm and 0.5–1 μm, respectively, while also narrowing the particle size distribution (Figure 1b,c). Note that the particle size distribution is generated by approximating the particles as spherical. The effects of ball milling on the nanopore and atomic structure of the carbons were monitored using Raman spectroscopy. Raman spectroscopy results confirm that there are no significant structural changes due to ball milling (Supporting Information Figure S1).

The C/S cathodes were prepared by melt-infiltrating the differently ball-milled carbons with sulfur using a C/S mass ratio of 1:1 (confirmed by thermogravimetric analysis (TGA) measurements, Supporting Information Figure S2, and by gas sorption analysis in our previous study [28]). The galvanostatic (dis)charge profiles (GCPL) at a rate of C/10 are presented in Figure 1d. A single voltage plateau is observed in all profiles (Figure 1d), confirming the solid-state conversion mechanism, regardless of carbon particle size [1, 6, 12, 18, 22]. By reducing the particle size (by up to a factor of eight), a significant decrease in overpotential is observed, accompanied by a nearly twofold increase in specific discharge capacity (capacity per gram of S). The rate performance was further evaluated at various discharging/charging rates of C/40, C/20, C/10, C/5, and C/2.5 for all the particle sizes (Figure 1e). Across all tested rates, cathodes incorporating smaller carbon particles consistently outperform those with larger ones, demonstrating enhanced sulfur utilization and improved rate performance. At a rate of C/2.5, the cathodes with the smallest carbon particles achieved a specific capacity of approximately 600 $mAh\,g_s^{-1}$, compared to only about 300 $mAh\,g_s^{-1}$ for those with larger particles. This particle size-performance relation cannot be attributed to cathode nanostructure differences, as the

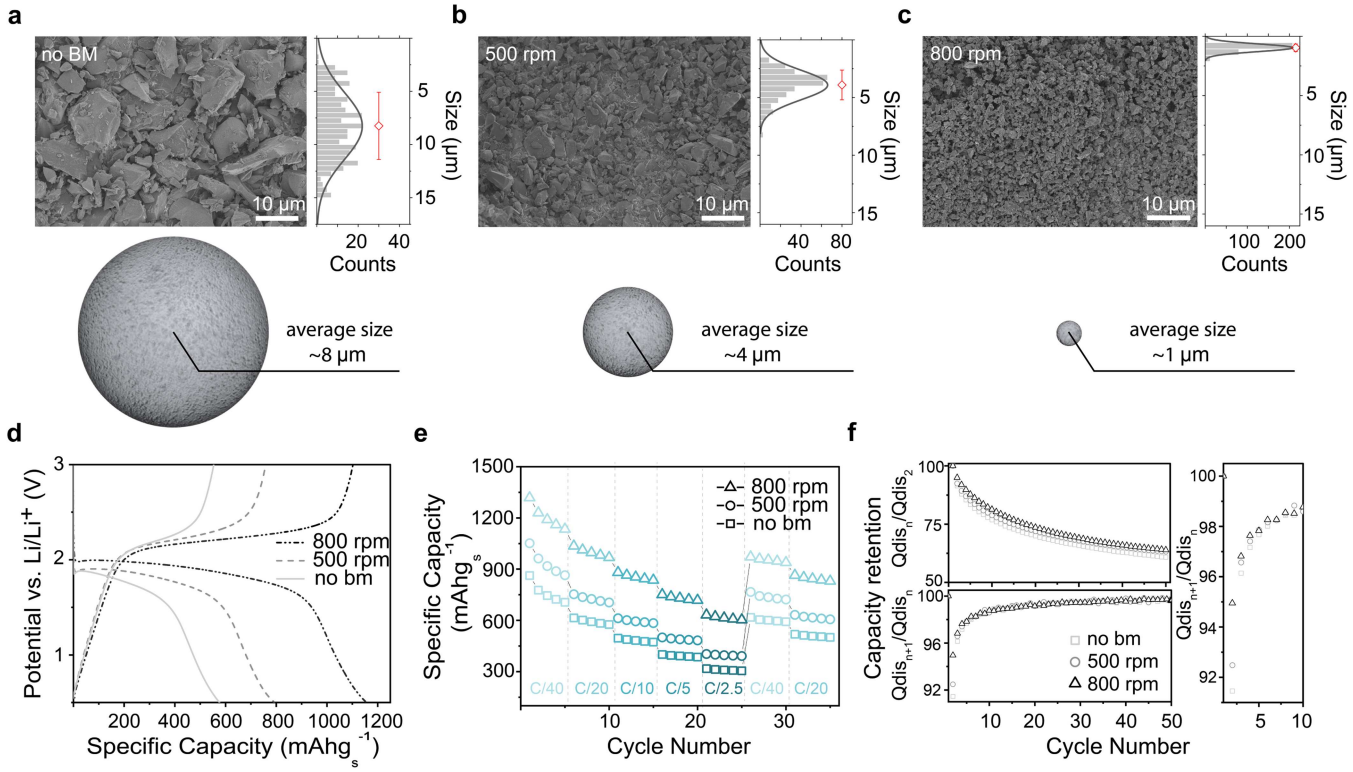

FIGURE 1 | Electrochemical performance as a function of carbon particle size. Scanning electron micrographs of (a) pristine 1-1 S-melt infiltrated carbon particles, (b) after 500 rpm ball milling, (c) and after 800 rpm ball milling. The size distributions are given on the right side of each micrograph; they become narrower with increasing ball-milling intensity. The average sizes are given below the micrographs; the spherical particle sketches are representative and drawn to scale. (d) The GCPL curves of the electrodes with differently ball-milled carbons are indicated as color tones and line style. The light gray continuous line represents the non-ball-milled particles with an average size of 8 µm, the dashed gray line represents the 500-rpm ball-milled particles with an average size of 4 µm, and the dash-dotted black line represents the 800-rpm ball-milled particles with an average size of 1 µm. Smaller particles give lower overpotentials and higher capacities. (e) The specific discharge capacities of the 800-rpm ball-milled (triangle shape), 500-rpm ball-milled (sphere shape), and non-ball-milled (square shape) carbon particles are given for the rates of C/40, C/20, C/10, C/5, and C/2.5. (f) Capacity retention as a function of cycling number, at the rate of C/10. The upper graph shows the ratio of the discharge capacity of the *n*th cycle over the discharge capacity of the 2nd cycle; the lower graph shows the ratio of the discharge capacities of the *n*th cycle over the previous cycle, with the graph on the right side being a zoomed version. Regardless of the particle size, there is a more distinct capacity fading in the first 5–10 cycles.

nanostructure and sulfur loading remain comparable after ball milling (Supporting Information Figures S1–S2). The relative capacity changes across different rates are similar for all particle sizes, indicating that sulfur utilization is consistently better with smaller particles, but not necessarily the kinetics.

Capacity retention was calculated during cell cycling between 0.5 and 3.0 V at a C/10 rate (Figure 1f and Supporting Information Figure S3 for the gravimetric and total capacities). The results are presented in two formats: (1) discharge capacity retention relative to the second discharge capacity (Q_{disn}/Q_{dis2}), excluding the first discharge due to CEI formation (upper graph), and (2) capacity retention relative to the preceding cycle's discharge capacity (lower graph). A more rapid capacity loss is observed during the initial 5–10 cycles, particularly in cells with the smallest carbon particles in the cathodes. Potential contributors to the observed capacity fade include CEI restructuring, interfacial side reactions, and mechanically induced effects. In this work, we attribute the more pronounced capacity fade in electrodes composed of smaller particles primarily to an increased loss of active sulfur species resulting from weaker effective confinement. This reduced confinement facilitates the diffusion of sulfur and intermediate polysulfide (PS) species out of the carbon host during the early discharge cycles, simultaneously leading to irreversible reactions with the carbonate solvent and, thus, loss of electrochemically active material and associated capacity fade. Across all particle sizes, the discharge capacity reaches a plateau after approximately 30–40 cycles, followed by minimal fading thereafter. Moreover, capacity fading is evident not only during continuous cycling at C/10 but also during rate capability measurements at any rate. Notably, the fading is more pronounced at lower current densities (C/40 and C/20), which may be linked to slower side-reaction rates driven by polysulfide shuttling and polysulfide reactions at the anode.

GITT measurements, along with the analysis of voltage relaxation times, provide additional insights into the evolution of overpotentials and mass transport kinetics during cycling [50, 51]. The cells with cathodes of different particle sizes were cycled between 0.5 and 3.0 V at a rate of C/10. Every 100 $mAhg_s^{-1}$ of capacity, the cells rest for 2 h at open-circuit

voltage (OCV). The absence of a voltage plateau at approximately 2.3 V versus Li/Li^+ during the first discharge confirms the in situ CEI formation and subsequent solid-state S/Li_2S conversion in the carbonate system [12, 18, 52] (Figure 2a–c). Both the shapes and overpotentials of the first discharge change significantly with the carbon particle size. For the non-ball-milled carbon, the initial discharge reveals a high overpotential and a sloped, hump-like profile instead of a well-defined plateau (Figure 2a). As the particle size decreases, the discharge profile becomes flatter, with significantly reduced overpotentials (Figure 2b,c). In the subsequent cycles, the overpotentials become comparable across all particle sizes and approach the equilibrium voltage near 2.1 V versus Li/Li^+ (Figure 2d,e,f) [12, 18]. The curves show the typical shape of solid-state S/Li_2S conversion in microporous carbons and carbonate electrolytes. Despite this similarity in overpotentials, the capacity differs by approximately 600 mAh_s^{-1} across the samples. These relations between overpotentials and particle size suggest that the CEI/Li_2S formation during the first discharge may be mass-transport-limited, while the subsequent solid-state S/Li_2S conversion is not.

The relaxation time constants τ, approximated by taking $1/e$ values of the normalized time-dependent potential relaxation

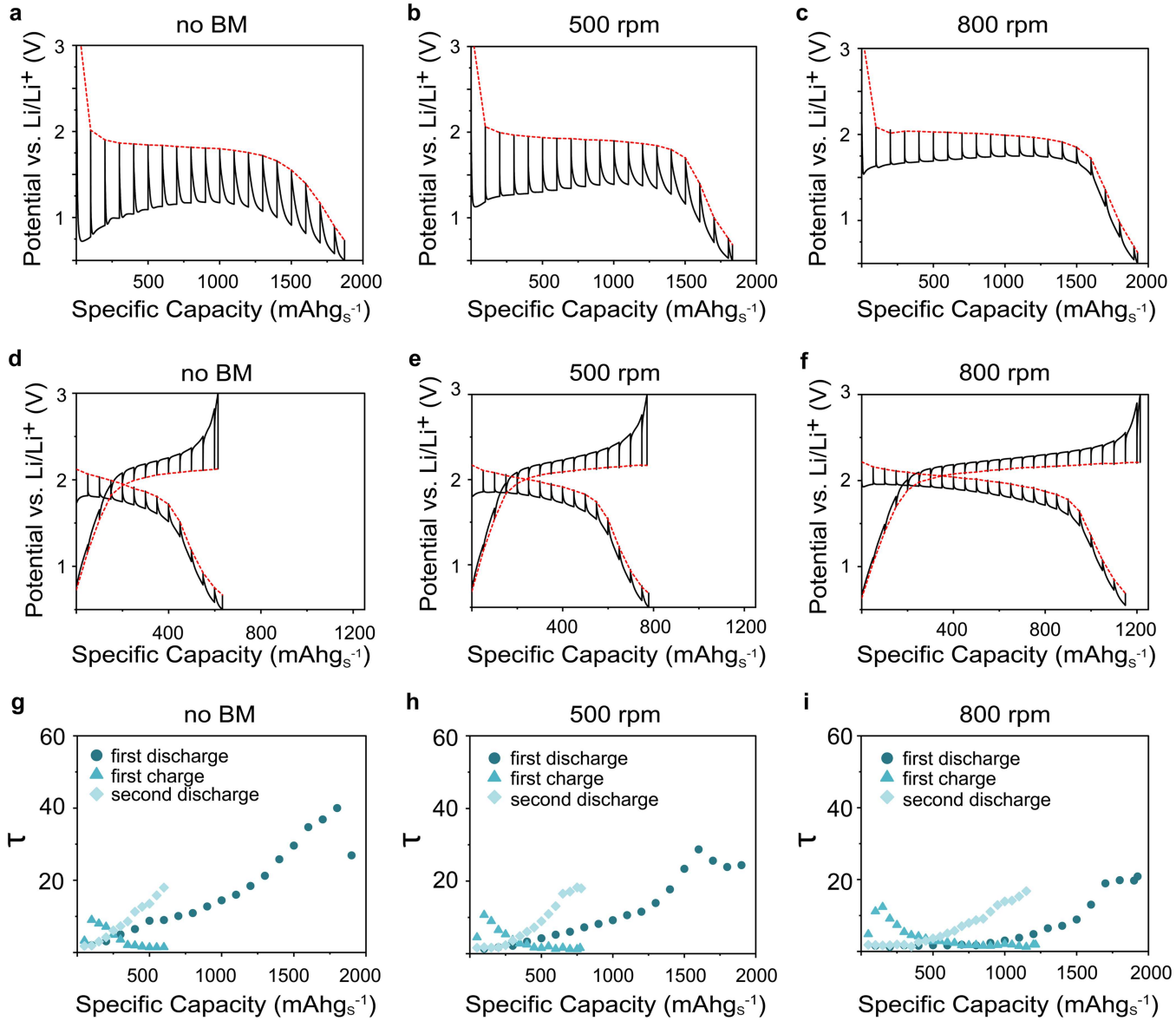

FIGURE 2 | Quantifying overpotentials and relaxation time constants using the galvanostatic intermittent titration technique (GITT). The GITT curves during the first discharge are shown for electrodes with (a) non-ball milled, (b) 500-rpm ball-milled, and (c) 800-rpm ball-milled particles, respectively. The corresponding GITT curves for further cycling, first charge, and second discharge, are presented in (d), (e), and (f), in the same order. All electrodes have a C/S ratio of 1, and the cycling rate is C/10. The red curves serve as a guide to the eye, connecting the relaxation voltages after 2 h of open circuit voltage (OCV). Despite significant differences during the first discharge, overpotentials and relaxation times become comparable in the subsequent cycles. Panels (g–i) show the relaxation time constants, approximated by 1/e values at normalized relaxation voltage curves during the OCV periods of the GITT measurements ($1-1/e$ during discharge and $1/e$ during charge). During the first discharge, electrodes with larger carbon particles exhibit time constants up to three times higher. In the following cycles, the relaxation time constants are comparable despite the eight-fold difference in particle size.

curves (Supporting Information Figure S4), can provide further evidence for that hypothesis. They are often linked to the rate of mass transport during cycling [53]. The most pronounced differences in relaxation times occur during the CEI formation process in the first discharge: the smallest particles exhibit relaxation times significantly lower than those of the largest (non-ball-milled) particles (Figure 2g–i). This is consistent with the approximation $\tau \propto L^2/D$ for mass transport into spherical particles, where L is the particle diameter, and D is the diffusivity, indicating enhanced transport kinetics in smaller particles. Note that in a recent study using *operando* small-angle neutron scattering, we indeed show that CEI formation occurs within the bulk of the nanoporous particles, and not only on their outer surface [28]. In the subsequent cycles following CEI formation, the relaxation times decrease and are comparable across all particle sizes, despite the eight-fold size difference in L. Additionally, across all samples, the relaxation times become lower during sulfur lithiation and higher during Li_2S delithiation, which may be linked to changes in charge transfer rates during charge and discharge [1, 52].

Overall, electrochemical and GITT data suggest a complex interplay between particle size, mass transport, CEI formation, and overall electrochemical performance. Smaller particles outperform larger ones at all tested rates, exhibiting up to a 2-2.5-fold increase in specific capacity. The distinct overpotentials and relaxation time differences during the first discharge imply that the in situ CEI/Li_2S formation is mass-transport-limited. Possible contributions to mass transport limitation include Li^+ transport or diffusion of reduced sulfur species (polysulfides). However, Li^+ transport also governs the solid-state sulfur conversion in subsequent cycles, where no significant particle-size-dependent differences in relaxation behavior are observed (Figure 2d–i). This suggests that Li^+ diffusion is unlikely to be the dominant rate-limiting factor during the first discharge. Instead, it may be related to PS diffusion and the chemical reactions between PS species and carbonate molecules, leading to the formation of CEI components, such as lithium ethylene monocarbonate and others [11]. However, distinguishing the individual contributions to mass transport limitation is challenging and requires further systematic studies. The particle-size independent timescales for mass transport during further S/Li_2S solid-state conversion, along with the differences in capacities, may imply a non-uniform distribution of CEI/active material within the particles. Larger particles may be incompletely filled with Li_2S/CEI after the first discharge, leading to incomplete sulfur utilization.

These findings highlight the significance of the irreversible CEI/Li_2S structure formation after the first discharge. Heterogeneities within particles of different sizes may explain the differences in observed capacities. To address this, we next examine the elemental distribution across a single discharged C/S particle using cryo-STEM with EDS and EELS.

Our microscopy measurements aim to determine whether the observed differences in electrochemical behavior across particle sizes correlate with variations in the spatial distribution of sulfur or CEI/active material during cycling. TGA measurements performed on the respective melt-infiltrated carbon powders confirm efficient melt infiltration into the porous carbon matrix. Regardless of particle size, all sulfur was found to reside within the nanoporous carbon particles, with no significant surface sulfur detected. Sulfur contents were 48.5 mass%, 49.0 mass%, and 49.7 mass% for non-ball milled, 500-rpm ball milled, and 800-rpm ball milled particles, respectively (Supporting Information Figure S2).

To spatially resolve CEI components and discharge products, EDS and EELS were conducted under cryo-vacuum conditions, minimizing electron beam- and air- induced damage [33]. For sample preparation, non-ball-milled AC08 particles were extracted from an electrode after the first discharge by gentle scratching and transferred to carbon tape on a sample holder. A large particle, potentially exhibiting the most pronounced mass transport effects, was selected (Figure 3a, left), and its central region was milled using a focused ion beam with the sample under cryo conditions (cryo-FIB) after coating with a protective platinum layer. The several μm thick lamella was then transferred to a TEM grid (Figure 3a, middle) and thinned to a 100–200 nm window, as confirmed by electron transparency and the EELS t/λ values (Figure 3a, right). Additional details on sample preparation and characterization are provided in the Methods section.

The cryo-EDS analysis of the cryo-FIB-prepared lamella reveals a relatively homogeneous sulfur distribution within the studied area (about 2 μm deep from the particle surface), with only a weak gradient in concentration (Figure 3b,c). It is not possible to definitively determine the origin of the detected sulfur; it may arise from discharge products (Li_2S, Li_2S_x), CEI components (thiocarbonates), or residual unconverted sulfur. As LiF is one of the known components of the CEI in carbonate-based electrolytes [1, 2, 7, 12, 21], the fluorine concentration is assumed to be directly related to the LiF and thus CEI distribution within the particle [2, 54]. We find that the LiF concentration increases towards the particle surface. Significant amounts could only be detected to a depth of 1 μm beneath the particle surface (Figure 3d).

STEM-EELS provides complementary high-resolution elemental and chemical bonding information. A line-scan (Figure 3e) reveals the presence of LiF, as identified by its characteristic core-loss signature at 62–69 eV (Figure 3f; see also Supporting Information Figure S5). Although cryo-conditions mitigate electron beam-damage, Li_2S remains susceptible to beam-induced degradation in STEM-EELS, similar to certain organic CEI components [55]. However, STEM-EELS enabled the identification of sulfur or sulfur-containing species, based on the distinct core-loss spectrum recorded at about 200 nm depth from the surface (Figure 3f, reference spectra in Supporting Information Figure S5). Due to the low signal intensity, we cannot conclusively attribute the signal to unreacted bulk sulfur; contributions from other species, such as Li_2S_x, cannot be excluded.

Figure 3g compares the S and LiF concentration profiles along a 300 nm line scan. To compensate for thickness variations caused by FIB sectioning, all signal intensity integrals were normalized by the t/λ ratio, a relative thickness measure calculated from the zero-loss signal that is also plotted on the secondary axis to validate data quality. LiF and S concentrations show an inverse correlation: we observe a LiF peak within the first ~100 nm, where sulfur content is lowest. Beyond this region, sulfur levels generally increase toward the particle center, whereas the LiF content generally drops. These opposing trends reflect the complex processes governing CEI formation and sulfur conversion during the first discharge.

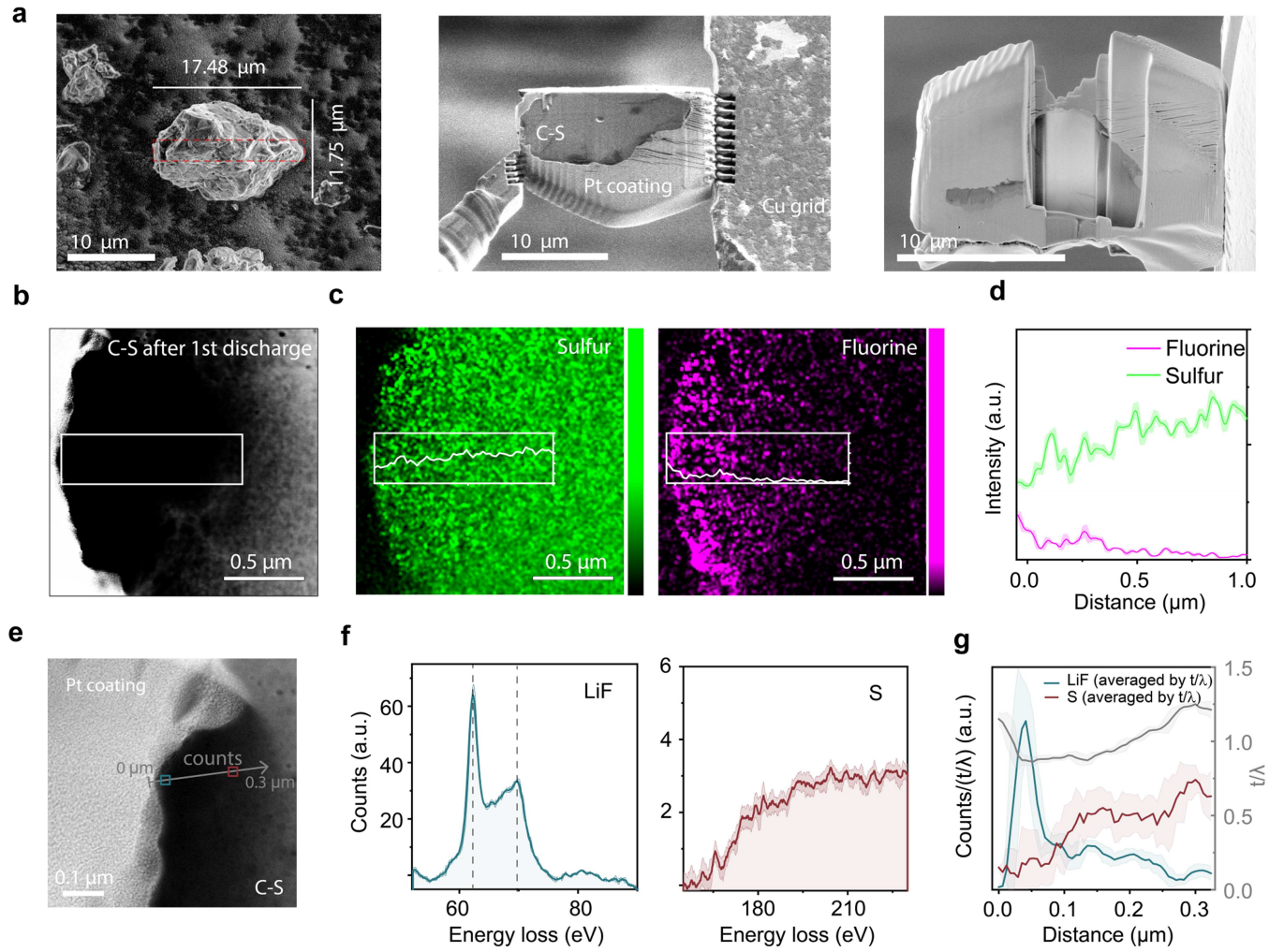

FIGURE 3 | Probing the intraparticular chemical composition using cryo-FIB/SEM, cryo-TEM/EDS, and cryo-STEM/electron energy loss spectroscopy (EELS). (a) Lamella preparation for cryo-EDS and cryo-EELS. An electrode with non-ball-milled carbon particles was scratched off onto carbon tape after the first discharge. The selected particle was coated with Pt, and a several-micron-thick lamella was extracted from the particle center (marked in red in a-left) using cryo-FIB-SEM. After transfer to a Cu TEM grid, the lamella was further thinned using cryo-FIB-SEM until a final thickness of 100–200 nm was achieved (image on the right). (b) STEM micrograph of the lamella window. The white-marked area indicates the region used for quantitative EDS net intensity analysis of the discharged non-ball milled particle. (c) EDS maps for sulfur K-line (green) and fluorine K-line (purple) of the discharged non-ball-milled particle. Sulfur is distributed throughout the depth of the carbon particle, while fluorine is more localized toward and on the particle surface. (d) Quantitative EDS net intensity profiles for sulfur K-line (green) and fluorine K-line (purple), extracted from the regions marked in (c). We attribute the fluorine signal to LiF, detected at approximately 1 µm depth from the surface. (e) STEM micrograph showing the EELS line measurement areas. The blue and red squares indicate the locations where energy-loss spectra of LiF and sulfur were collected, respectively. (f) EELS of sulfur L-edge (red) and Li K-edge (blue), recorded at marked points along the line marked in (e). The t/λ values (gray) confirm consistent measurement quality across the 300 nm scan length. The data show a lithium K-edge which can be attributed to LiF phase within the first 100 nm, followed by an inverse distribution trend between sulfur and LiF. (g) Left: Energy-loss spectrum of Li K-edge, with characteristic peaks at 65–68 eV for LiF phase, measured at ~50 nm depth. Right: Core-loss spectrum of sulfur L-edge at ~200 nm depth, showing a characteristic shoulder starting at ~160–165 eV, with overall lower intensity, indicating reduced sulfur content.

The presence of LiF, typically formed electrochemically at the carbon/electrolyte interface, appears most pronounced near the particle surface, where electrolyte accessibility is highest. The inverse concentration profiles of LiF and sulfur species suggest that LiF preferentially forms in areas where sulfur has already been consumed or is absent [11], consistent with limited mass transport deeper into the particle interior. Together, the EDS and EELS data indicate that CEI formation extends beyond a thin surface layer into the particle bulk, with a pronounced LiF gradient pointing to diffusion-limited growth in larger particles.

The ex situ cryo-TEM micrographs in Figure 4a–c (also Supporting Information Figure S6) of the discharged electrodes with 800-rpm ball-milled particles provide visual insights into the CEI morphology on the particle surface. Note that in contrast to the particle cross-section in Figure 3, there was no FIB-milling involved. Qualitatively, the contrast differences on the

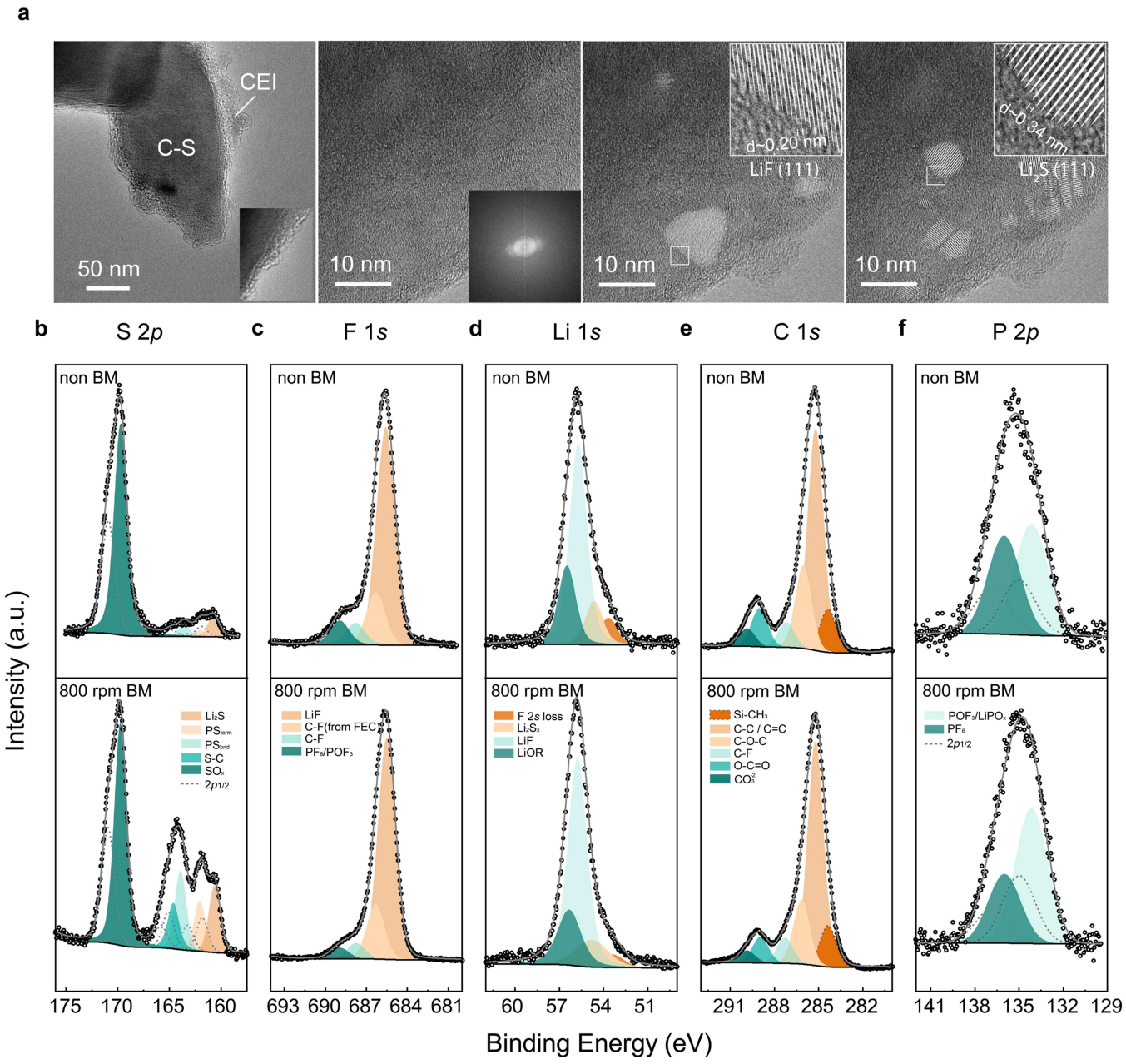

FIGURE 4 | Transmission electron microscopy (TEM) and X-ray photoemission spectroscopy (XPS) measurements to probe the particle surface. (a) TEM micrographs of the discharged only 800-rpm ball-milled C–S particles without binder. The images suggest that the CEI forms a heterogeneous layer composed of crystalline phases, solid clusters, and organic components. Crystalline Li_2S (111) and LiF (111) reflections are marked as FFT filtered images on a discharged particle. (b–f) High-resolution XPS spectra of the non-ball milled cathode (top row) and the 800-rpm ball milled cathode (bottom row) in the discharged state after the first cycle: (b) S 2*p*, (c) F 1*s*, (d) Li 1*s*, and (e) C 1*s* (Si-CH_3 contribution is due to the tape on which the samples were placed), and (f) P 2*p*. Circular dots represent the experimental data, the gray line corresponds to the composite fitted spectrum, and the black line indicates the background. FFT, fast Fourier transform.

surface of the particles reveal that the CEI is not a homogeneous film on the particle surface and has a varying thickness of several tens of nanometers. Lattice fringes of crystalline Li_2S and LiF features were identified. Using a fast Fourier transform (FFT) analysis, the lattice fringes could be assigned to the (111) plane of LiF [56] and the (111) plane of Li_2S [12, 18]. These nanocrystalline phases are embedded in the CEI layer on the particle surface, which likely consist of additional organic and inorganic phases [6, 12, 20]. Overall, these observations point to a structurally complex and non-uniform CEI layer on the particle surface, which may contribute to the limited rate performance of our Li–S system. Heterogeneous, particulate surface structures are also visible in the SEM micrographs after the first discharge, with slight differences depending on particle size (Supporting Information Figure S7).

To further corroborate the chemical composition of the discharged particle surfaces, XPS was performed for the non-ball-milled and 800-rpm ball-milled samples at the end of the first discharge. Prior to analysis, the cathodes were carefully rinsed with DMC to remove excess surface salt deposits and enhance the signal from the particle surfaces. Figure 4b–f presents the

high-resolution spectra for the different elements along with their deconvolution. Supporting Information Table S1 shows the atomic concentrations of the detected elements, and Supporting Information Tables S2–S6 summarize peak assignments, their corresponding sources, and the FWHM values. Both cathodes exhibit the same chemical contributions for each element. The main difference lies in the S 2*p* spectra, which display five distinct components. Three peaks are associated with reduced sulfur species: Li_2S at 160.7 eV, and polysulfides showing two characteristic signals corresponding to terminal sulfur (162.0 eV) and bridging sulfur (163.7 eV) [57–59]. In the ball-milled sample, these three contributions account for 33% of the total sulfur signal, compared with only 16% in the non-ball-milled electrode. The fourth component at 164.6 eV corresponds to C–S bonds, originating from interactions between solvent molecules and polysulfides. Finally, the peak at 169.7 eV is assigned to oxidized sulfur species, most likely Li_2SO_4, due to its high binding energy. This signal has the highest intensity in both samples but likely results from surface reactions within the CEI and typically decreases in the bulk of the electrode [1, 60].

The F 1*s* spectrum contains four distinct contributions. The most prominent peak, at 685.5 eV, is assigned to LiF, which has its counterpart in the Li 1*s* spectrum at 55.7 eV. LiF originates from both the decomposition of fluoroethylene carbonate and the reaction of $LiPF_6$ with DMC [58]. The latter pathway also generates POF_3, which appears in the F 1*s* spectrum at 688.9 eV (overlapping with the PF_6 anion signal) and in the P 2*p* spectrum at 134.2 eV. The other two contributions in the F 1*s* spectrum are assigned to the C–F bonds (from FEC) at 686.3 eV and at 687.8 eV (from $-CHF–OCO_2$-type compound). The $-CHF–OCO_2$ species also originate from FEC decomposition and are accompanied by a corresponding peak in the C 1*s* spectrum at 287.2 eV (C–F) and at 289.9 eV (CO_3^{2-}) [61, 62]. Another important CEI component is lithium carbonate, formed via DMC decomposition, which is observed at 289.9 eV in the C 1*s* spectrum and at 56.3 eV in the Li 1*s* spectrum. Overall, XPS confirms the presence of LiF and Li_2S as key components of the CEI layer on the particle surface, with a higher Li_2S concentration observed in the ball-milled samples. To what extent surface-Li_2S contributes to the reversible capacity remains to be clarified. However, given their small overall amount, as determined by XRD (see Ref [28]), we believe their contribution is negligible.

An estimate of residual sulfur can be derived from the ratio of the bridging to terminal sulfur peak areas in the S 2*p* spectrum. Assuming Li_2S_2 as the dominant polysulfide, as terminal-to-bridging sulfur area ratios exceeding 2:1 would be inconsistent with the measured spectra, the deconvolution of the CEI sulfur signal yields approximate contributions of 25% residual sulfur, 45% Li_2S_2, and 30% Li_2S. It should be emphasized that these values are semi-quantitative and representative only of the CEI region probed by XPS [57].

STEM-EELS confirms the presence of sulfur-containing species at the particle surface at nanoscale resolution. In contrast, XPS offers higher chemical-state sensitivity for sulfur and allows quantitative differentiation between reduced sulfur species and oxidized sulfur compounds. However, this information is only true for the outer surface of the CEI layer on the C/S particle (approx. 5–10 nm).

The EDS and EELS results indicate an increased presence of LiF (i.e., the CEI) in the first 100 nm beneath the particle surface; a detectable concentration extends to about 1 μm underneath the surface. The sulfur distribution, on the other hand, is relatively homogeneous across the particle inside. CEI components and their defect-rich grain boundaries possess favorable Li-ion conductivity [2, 54, 56, 63–65] but lack electron conductivity, while the carbon host shows the opposite behavior. Therefore, we hypothesize that regions where sulfur, carbon, and CEI species are in close proximity serve as electrochemically active regions after the initial formation cycle. These regions likely enable enhanced mass transport and charge transfer kinetics due to the presence of triple-phase boundaries (TPBs, Figure 5a). TPBs have been recognized as critical for efficient electrochemical conversion in all-solid-state Li–S batteries [66–68] and Li_2S nucleation in glymes [69, 70]. Considering our findings, we propose a similar mechanism in our system, with efficient solid-state S/Li_2S conversion only in regions where sulfur, carbon, and CEI components co-locate.

To further support this hypothesis, we performed a plausibility check by correlating rate-dependent capacities with the estimated fraction of electrochemically active particle volume across different particle sizes. Assuming spherical particle geometry with a mean size as shown in Figure 1a–c and LiF presence restricted to the 1 μm outermost layer, we approximated the relative active region volume across the different particle sizes (Figure 5b). For an average particle size of 8 μm, this volume fraction is approximately 0.6. By downsizing the particles, the ratio increases. For the 800-rpm ball-milled particles, we assumed a maximum volume fraction of 1.

Using the experimentally measured rate performance of 800-rpm ball-milled particles as reference, we calculated the expected rate capability of larger particles by scaling with the corresponding active region volume fractions (Figure 5c–e). The resulting predicted capacities (red curves) are in reasonable agreement with experimental data (blue curves), capturing the general trend. This analysis should be seen as a simplified consistency check, and the assumed active region thickness of 1 μm is admittedly arbitrary. However, it provides a useful qualitative benchmark. Importantly, the key indicator is not the absolute capacity values that overlay, but rather the fact that the rate-dependent capacity curves show the same relative change across all particle sizes. Taken together, these observations suggest that performance is not solely determined by mass transport limitations but is strongly influenced by the fraction of sulfur that is electrochemically accessible after the first discharge. Thus, smaller particles, with a larger proportion of electrochemically active material, enable higher capacities, while larger particles contain inactive regions that limit capacity.

In our previous study, completed with larger carbon particles of varying pore sizes, we proposed that delithiation is slower than lithiation, leading to capacity limitations during fast charging [28]. However, the Li–S batteries could still be discharged at higher rates. To explore whether particle size influences this asymmetry, we performed a charge-rate test using the smallest particles. Cells were discharged at a fixed rate of C/5 while charged at varying rates. Similar to the results with larger particles, the discharge capacity follows the previous charge capacity (Figure 5f). However, under slow-discharge/fast-

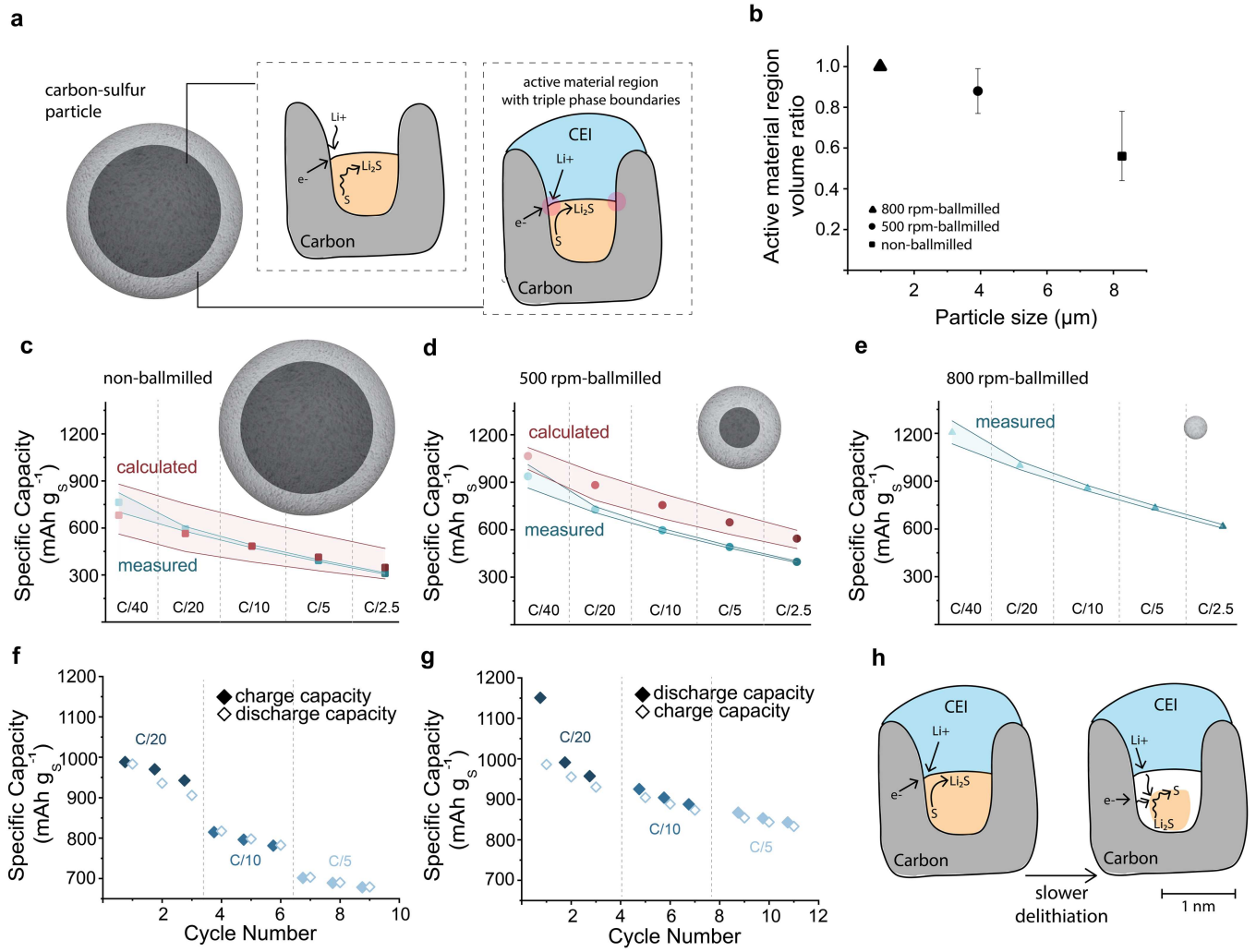

FIGURE 5 | Particle size-dependent rate and capacity limitations in solid-state S/Li_2S conversion. (a) Schematic illustration of electrochemically active regions with triple-phase boundaries, which are preferably located near the particle surface. Light-colored regions in the spherical particle represent more active zones, while darker regions correspond to less active areas. (b) Estimated ratio of the active material region volume to the total particle volume as a function of particle size. For 1 μm-sized particles, this ratio approaches unity. (c, d) Predicted rate performance (red curves) for non-ball milled and 500-rpm ball milled carbon particles, respectively, based on their active volume fractions. The predictions are derived from the measured performance of 800-rpm ball-milled particles, shown in (e) as the blue curve. (f) Specific capacities of 800-rpm ball-milled carbon for constant discharge rate (C/5) and varying charge rates (C/20 to C/5). Filled symbols represent charging capacities; unfilled symbols show the subsequent discharge capacities. (g) Specific capacities for constant charge rate (C/5) and varying discharge rates (C/20 to C/5). Filled symbols represent discharge capacities; unfilled symbols show the subsequent charge capacities. Both (f) and (g) confirm the dependence of performance on the charge rate. (h) Schematic illustration of the delithiation process, where sulfur volume shrinkage during charging is suggested to slow down charge transfer, making charging the rate-limiting step for all particle sizes.

charge conditions, the overall capacities decreased (Figure 5g), confirming delithiation as the limiting process. These results demonstrate an intrinsic asymmetry between lithiation and delithiation, but do not by themselves identify the underlying limiting mechanism. Based on our earlier mechanistic analysis using GITT, EIS, and galvanostatic cycling with a systematic variation of nanopore size and sulfur pore filling, the observed overpotential and relaxation trends were inconsistent with dominant Li^+ mass-transport limitations and instead point to an interfacial kinetic constraint at the carbon/active material/CEI interface during Li_2S/S conversion [28]. Consistent with this interpretation, even at matched charge-discharge rates, the specific charge capacities remained lower than their corresponding discharge capacities, indicating that charge-transfer resistance, particularly during charging [70], persists as a limiting factor independent of particle size. We speculate that this intrinsic limitation originates from the swelling and shrinking of active materials within the pores during cycling [1, 52], a nanoscale phenomenon that cannot be mitigated by particle downsizing alone.

3 | Conclusions

In conclusion, this study highlights the critical role of particle size and its impact on in situ CEI formation in governing electrochemical performance in Li–S batteries with solid-state conversion in nanoporous carbons. Smaller particles deliver

higher specific capacities across various cycling rates. GITT and relaxation time analyses reveal that mass transport limitations, particularly pronounced in larger particles, are most impactful during the first discharge, thereby affecting the CEI/Li_2S formation.

To probe the structure of CEI and active materials, we employed cryogenic electron microscopy to overcome the materials' intrinsic beam and vacuum sensitivity. TEM results in combination with EDS and EELS show the inhomogeneity of LiF, Li_2S, and S on the surface and across the inside of an individual discharged particle. LiF, as an important CEI component tends to concentrate within the first micron from the particle surface instead of forming solely a thin film on the surface. Triple-phase regions, co-locating active material (S/Li_2S), carbon, and LiF, appear to function as electrochemically active regions. Their spatial extent decreases with increasing particle size, likely because of mass transport limitation in the first discharge, limiting the effective reaction volume and contributing to reduced capacities and rate capability.

Taken together, these results imply that the performance is ruled by a multiscale interplay of rate and capacity-limiting mechanisms. Mass transport during the first discharge determines CEI formation and internal distribution of active material, while charge transfer resistance during charging remains a rate-limiting factor independent of particle size. These findings suggest two design pathways for improving performance: (i) Tailoring particle size and morphology to promote uniform CEI throughout the particle, and (ii) enhancing charge transfer kinetics during solid-state conversion through controlled nanopore structures (e.g., smaller nanopores), as demonstrated in previous work [28] or surface functionalities.

Our results establish the importance of in situ CEI/Li_2S formation for determining electrochemical performance, but the stability of the CEI and its role in capacity fading during the initial cycles remain open questions. Addressing these aspects, together with the cathode design strategies identified here, will be essential for advancing Li–S batteries with solid-state conversion in confinement.

4 | Experimental Section

4.1 | Materials

Elemental sulfur (powder, 99.98% trace metals basis, Sigma Aldrich, and without any further processing) and microporous activated carbon (dried at 200°C under vacuum overnight), MSP20 (denoted as AC08), were mixed manually with different weight ratios in an agar mortar. AC08 has a mean pore size of about 0.8 nm, and is provided by Kansai Coke and Chemicals and Kuraray Chemicals Co. The AC08-powder was used as-received and after ball milling under two different conditions. The powder was milled using a Fritsch Planetary Micro Mill (Pulverisette 7) with tungsten carbide balls (1.6 mm in diameter) without a solution medium. We used rotation speeds of 500 rpm and 800 rpm and milled for 30 min with a 10 min resting period four times (160 min). The ball-to-powder mass ratio was kept at 10. Before melt-infiltration, the non- and ball-milled carbons were heated to 200°C overnight to get rid of the bound water in the pores. Then they were mixed with elemental sulfur at a sulfur-to-carbon mass ratio of 1:1 in an agar mortar. The prepared mixture was melt-infiltrated at 155°C for 7–8 h in a sealed evacuated glass oven (Büchi). The final sulfur mass content was verified by weight and through thermogravimetric analysis (TGA).

The electrodes were prepared by mixing carbon composite with polyacrylic acid (PAA, Mv 450.000, Sigma Aldrich, 10 mass% suspension in water) at a 9/1 mass ratio with drops of additional ethanol (≥ 99.8%, Sigma Aldrich) and water for better miscibility. The slurries were mixed with IKA overhead stirrer (IKA) at maximum speed (10 min) together with a vortex mixer (5 min). The resulting slurry was coated on Aluminum foil as a 100–200 μm thick film using a Doctor Blade coater and dried at 50°C under vacuum (10 mbar) for 2 h. The film electrodes coated after drying have a thickness in the range of 20–50 μm.

After drying, the electrodes were cut (puncher diameter 13 mm), resulting in a geometrical surface area of 1.32 cm^2. The sulfur loadings varied from 1.7 to 2.5 $mg_s cm^{-2}$. As an electrolyte, a solution of 1 M lithium hexafluorophosphate ($LiPF_6$) in fluoroethylene carbonate (FEC): dimethyl carbonate (DMC) (by volume 1:4) was used, and E/S ratio is kept at 20. All solvents were dried with molecular sieves (3 Å, beads, 8–12 mesh, Sigma Aldrich), and the salt was dried under vacuum overnight.

4.2 | Methods

TGA measurements were performed at the National Institute of Chemistry, Slovenia, to determine the sulfur content. The measurements were conducted on a STA 449 F3 Jupiter under an argon atmosphere, in an alumina crucible (Al_2O_3) with a heating rate of 10°C min^{-1} up to a maximum temperature of 900°C.

Raman spectroscopy was conducted at INM Saarbrücken with a Renishaw in Via Raman microscope employing an Nd-YAG laser (532 nm) at a power of 799 μW. For each sample, spectra from 10 points were recorded with cosmic ray removal treatment with 10 s exposure time and three accumulation periods. Before each measurement, the system was calibrated with a silicon wafer that was later used as a sample holder.

Scanning electron microscopy (SEM) images for the particle size analysis were recorded after ball milling followed by drying and S-melt infiltration at 1-1 S-C mass ratio. The SEM samples of electrodes after discharge were washed with diethylene glycol dimethyl ether (2 G, anhydrous, 99.5%, Sigma Aldrich) and dried under vacuum for 5–10 min. All steps were completed in an Ar-filled glovebox, and the samples were transferred inside a vacuum transfer holder. All scanning electron micrographs were taken with a Hitachi SU-8200 at 1 kV acceleration voltage with backscattered and secondary electron detectors. The particle size analysis was completed for all S-infiltrated carbon powders with or without ball milling, based on 300 particles randomly selected in FiJi from scanning electron micrographs of different regions. Considering the heterogeneous shapes, the diameters were calculated from an assumed spherical shape. After masking as spheres (an example given in Supporting Information Figure S8) and thresholding, the diameters were calculated from the areas, assuming a spherical shape represented as Gaussian size distribution graphs with illustrated standard deviations.

All custom-built coin-cell-type electrochemical cells were assembled under an inert atmosphere in an argon-filled glovebox. The cells consisted of an aluminum current collector (18 mm in diameter), coated film C/S cathode, a both-side-ceramic-coated polypropylene separator (20 mm in diameter), and a metallic lithium anode (18 mm in diameter, 110 μm thick, FMC Lithium corporation). The electrolyte-to-sulfur-ratio was kept at 20 $\mu L mg_s^{-1}$ to ensure continuous separator wetting.

All electrochemical characterization was performed with a Biologic VMP3 or MPG2 potentiostat/galvanostat. Galvanostatic cycling was done (also for capacity retention tests) between 3.0 and 0.5 V versus Li/Li^+ with a rate of C/10 (except for the rate performance tests). The rate capability tests investigating the effect of ball milling (or carbon particle size) started with formation discharge at C/10 and were followed by 5 discharge/charge cycles at each rate. Similarly, for the charge/discharge rate experiments, all cells were first discharged, and if needed, charged once at the rate of C/10. During the GITT (galvanostatic intermittent titration technique) measurements for every 100 $mAh g_s^{-1}$ capacity, the cells were rested at the OCV for 2 h until the relaxation voltage equilibrated. The relaxation voltage versus time indicates sufficient equilibration while maintaining experimental efficiency. The time-dependent potential relaxation during OCV was normalized and shown in Supporting Information Figure S4. From each curve, relaxation time constant values were approximated based on $1-1/e$ values during discharge and $1/e$ values during charge.

Cryo-FIB-SEM measurements were performed at ScopeM using a Helios NanoLab 600i dual-beam microscope (FEI/Thermo Fisher Scientific). A lamella was prepared for subsequent EELS, EDS, and TEM analysis after the first discharge of a non-ball-milled electrode. For that, the electrode was removed after the first discharge, and the active material was gently scratched onto a carbon tape in an argon-filled glovebox ($O_2 < 0.1$ ppm, $H_2O < 0.1$ ppm). All the sample handling was completed in an argon-filled glovebox to minimize exposure to air and moisture, including the transport, which is accomplished by a vacuum holder. Samples were subsequently transferred to the FIB-SEM instrument using an EM VCT100 vacuum cryo transfer system (Leica). The stage temperature during cryo-FIB-SEM operations was maintained at approximately −150°C under high vacuum conditions (pressure, ~$2e10^{-6}$ mbar). A single particle with a size of 15 μm (approximately in all directions) was selected for cross-sectioning. SEM imaging was performed whenever needed throughout the processes of particle selection, milling, and transfer of the lamella. It was conducted at 3 kV using a secondary electron detector (ETD or ICE, Thermo Fisher Scientific) with a SEM working distance of about 4 mm. Prior to the milling procedure and before cooling down the sample, the selected particle was coated with a platinum (Pt) protective layer of approximately 3–5 μm thickness. Pt was selected to deposit for both the protection of active material and to provide better contrast to the sample surface during TEM measurements. Initial milling was carried out at 30 kV with a Ga^+ ion beam, with currents adjusted based on the milling stage in a range of 1–10 nA, producing a lamella several micrometers thick to ensure mechanical stability of the window. The thick lamella was then transferred to a copper TEM lift-out grid (Lacey Carbon Type-A Copper TEM grid, TedPella, no. 01890) using a micromanipulator (EasyLift). Mounting the lamella to the manipulator and to the TEM lift-out grid was done through a redeposition welding process, as standard FIB-induced deposition is not possible under cryo conditions. A thin measurement window (2–5 μm in lateral size and ending with ~100–200 nm in thickness) was finally prepared by gentle thinning at progressively reduced ion beam acceleration voltages and currents, suitable for sensitive structures, by ensuring minimal damage. The final thickness was verified by both electron transparency at 2–3 kV and by monitoring τ/λ values during EELS acquisition in later stages. Finally, the mounted lamella on the copper grid was transferred back to the argon-filled glove box (EM VCT100 Vacuum cryo transfer system, Leica) for mounting to a cryo-vacuum TEM holder for the subsequent TEM, STEM, EELS, and EDS characterization under cryogenic conditions [71]. TEM measurements were carried out on a double Cs-corrected JEOL GrandARM operated at 300 kV (ETH Zürich) equipped with two large area SDD EDX detectors with 100 mm^2 active area; total solid angle: 1.6 sr for dual EDS and GATAN 965 GIF Quantum ER EELS Spectrometer/Imaging Filter, combined with Cryo Vacuum Transfer Holder by MelBuild, which is then cooled to −193°C by introducing liquid nitrogen (LN2). For the EDS and EELS analysis, the programs of Analysis Station (JEOL) and GMS3 (Gatan) were used, respectively. The integrals of the signals were calculated within these programs, and the results were presented as a moving average of 5.

For the ball milled particle, the TEM sample preparation was slightly different, since the particle is not larger than 1–2 μm, and preparing a lamella containing a single particle would be practically not possible. There are two sample preparation techniques: either the electrodes with the 800-rpm ball-milled particles were scratched off after the first discharge, or the ball-milled particles were discharged directly to remove the influence of the binder material on a glassy carbon disc. Details of the powder discharge are described in Ref [55]. Electrodes/particles were discharged to 0.5 V at a rate of C/10. The discharged electrode/particles were transferred to the TEM grid and measured directly. All transfer processes were conducted under cryo-vacuum conditions.

XPS was performed on both ball-milled (800 rpm) and non-ball-milled cathodes at the end of the first discharge. To avoid contamination, cells were disassembled in an argon-filled glovebox. The electrodes were rinsed with dimethyl carbonate (DMC) to remove residual surface salt and subsequently dried under dynamic vacuum overnight. After drying, samples were transferred to the vacuum transfer module of the Versaprobe 3 AD spectrometer to prevent air exposure. XPS measurements were conducted using a Versaprobe 3 AD system (Physical Electronics) equipped with a monochromatic Al Kα X-ray source (1486.6 eV) operating at 50 W. Spectra were collected at room temperature under ultra-high vacuum conditions (10^{-9} mbar). The X-ray beam size was set to 200 μm, and a 1 mm^2 area was scanned for each sample. A dual-beam charge neutralization system (1 V, 20 μA) was employed to mitigate surface charging effects, as the samples were mounted on non-conductive double-sided adhesive tape, ensuring accurate determination of binding energies. The analysis comprised both wide-range survey scans and high-resolution core-level spectra for phosphorus (P 2*p*), sulfur (S 2*p*), carbon (C 1*s*), oxygen (O 1*s*), and fluorine (F 1*s*). Survey spectra were acquired using a pass energy of 224 eV with an energy resolution of 0.8 eV, while core-level spectra were recorded at a pass energy of 27 eV

and a resolution of 0.05 eV. Spectral deconvolution was carried out using Voigt line shapes and a Shirley-type background subtraction, as implemented in the Ulvac-PHI Multipak software. Binding energy calibration was referenced to the Au $4f_{7/2}$ peak at 83.99 eV from a sputtered gold standard, ensuring accurate energy alignment across all measurements.

Author Contributions

Ayca Senol Gungor conducted experiments and data analysis of electrochemical characterization and electron microscopy. Sven Dunkel contributed the electrochemistry measurements and data analysis. Jean-Marc von Mentlen and Milivoj Plodinec carried out cryo-microscopy together with EDS and EELS. Christian Zaubitzer was responsible for lamella preparation with cryo-FIB microscopy. Volker Presser and Jean G. A. Ruthes carried out Raman spectroscopy. Francisco Javier García-Soriano and Alen Vizintin conducted the TGA and XPS measurements. Ayca Senol Gungor, Christian Prehal, and Vanessa Wood conceptualized the work. Ayca Senol Gungor and Christian Prehal wrote the initial version of the manuscript. All authors contributed to the results interpretation and revised the manuscript.

Acknowledgements

We acknowledge the funding for the ALISA project (project number 9359) provided by the m-ERA.NET network (part of the European Union's Horizon 2020 research and innovation program (under grant agreement No. 958174)), and the Slovenian Ministry of Higher Education, Science, and Innovation. AV further acknowledges financial support from the Slovenian Research and Innovation Agency (ARIS), research core funding P2-0423 and project GC-0004. This work was funded by the European Union (ERC-2022-STG, SOLIDCON, 101078271). Views and opinions expressed are, however, those of the authors only and do not necessarily reflect those of the European Union or the European Research Council Executive Agency. Neither the European Union nor the granting authority can be held responsible for them. ASG and JMM acknowledge the financial support for the ALISA project from the Swiss Federal Office of Energy SFOE. Additionally, ASG acknowledges the valuable support from Mario Mücklich (ETH Zürich). ASG, CZ, and MP recognize the support of ScopeM facilities. JGAR and VP acknowledge the financial support for the ALISA project from the German Federal Ministry for Education and Research (BMBF, 03XP0504A). Open Access funding provided by Paris Lodron Universitat Salzburg/KEMÖ.

Conflicts of Interest

The authors declare no conflicts of interest.

Data Availability Statement

The data that support the findings of this study are available at https://doi.org/10.5281/zenodo.17841176.

References

1. X. Chen, H. Ji, Z. Rao, et al., "Insight Into the Fading Mechanism of the Solid-Conversion Sulfur Cathodes and Designing Long Cycle Lithium–Sulfur Batteries," *Advanced Energy Materials* 12, no. 1 (2021): 2102774, https://doi.org/10.1002/aenm.202102774.

2. X. Chen, L. Yuan, Z. Li, et al., "Realizing an Applicable "Solid → Solid" Cathode Process via a Transplantable Solid Electrolyte Interface for Lithium–Sulfur Batteries," *ACS Applied Materials & Interfaces* 11, no. 33 (2019): 29830–29837, https://doi.org/10.1021/acsami.9b07787.

3. L. Wang, Y. Ye, N. Chen, et al., "Development and Challenges of Functional Electrolytes for High-Performance Lithium–Sulfur Batteries," *Advanced Functional Materials* 28, no. 38 (2018): 1800919, https://doi.org/10.1002/adfm.201800919.

4. G. Li, S. Wang, Y. Zhang, M. Li, Z. Chen, and J. Lu, "Revisiting the Role of Polysulfides in Lithium–Sulfur Batteries," *Advanced Materials* 30, no. 22 (2018): e1705590, https://doi.org/10.1002/adma.201705590.

5. J. Liu, H. Chen, W. Chen, Y. Zhang, and Y. Zheng, "New Insight Into the 'Shuttle Mechanism' of Rechargeable Lithium–Sulfur Batteries," *ChemElectroChem* 6, no. 10 (2019): 2782–2787, https://doi.org/10.1002/celc.201900420.

6. A. Rosenman, E. Markevich, G. Salitra, Y. Talyosef, F. Chesneau, and D. Aurbach, "Facile Synthesis and Very Stable Cycling of Polyvinylidene Dichloride Derived Carbon: Sulfur Composite Cathode," *Journal of the Electrochemical Society* 163, no. 9 (2016): A1829–A1835, https://doi.org/10.1149/2.0151609jes.

7. E. Markevich, G. Salitra, A. Rosenman, Y. Talyosef, F. Chesneau, and D. Aurbach, "The Effect of a Solid Electrolyte Interphase on the Mechanism of Operation of Lithium–Sulfur Batteries," *Journal of Materials Chemistry A* 3, no. 39 (2015): 19873–19883, https://doi.org/10.1039/c5ta04613k.

8. X. Ji, K. T. Lee, and L. F. Nazar, "A Highly Ordered Nanostructured Carbon–Sulphur Cathode for Lithium–Sulphur Batteries," *Nature Materials* 8, no. 6 (2009): 500–506, https://doi.org/10.1038/nmat2460.

9. J. Li, L. Gao, F. Pan, et al., "Engineering Strategies for Suppressing the Shuttle Effect in Lithium–Sulfur Batteries," *Nano-Micro Letters* 16, no. 1 (2023): 12, https://doi.org/10.1007/s40820-023-01223-1.

10. W. P. Wang, J. Zhang, J. Chou, et al., "Solidifying Cathode–Electrolyte Interface for Lithium–Sulfur Batteries," *Advanced Energy Materials* 11, no. 2 (2020): 2000791, https://doi.org/10.1002/aenm.202000791.

11. L. Wang, Y. Lin, S. DeCarlo, et al., "Compositions and Formation Mechanisms of Solid-Electrolyte Interphase on Microporous Carbon/Sulfur Cathodes," *Chemistry of Materials* 32, no. 9 (2020): 3765–3775, https://doi.org/10.1021/acs.chemmater.9b05027.

12. E. Markevich, G. Salitra, Y. Talyosef, F. Chesneau, and D. Aurbach, "Review—On the Mechanism of Quasi-Solid-State Lithiation of Sulfur Encapsulated in Microporous Carbons: Is the Existence of Small Sulfur Molecules Necessary?," *Journal of the Electrochemical Society* 164, no. 1 (2016): A6244–A6253, https://doi.org/10.1149/2.0391701jes.

13. B. Zhang, X. Qin, G. R. Li, and X. P. Gao, "Enhancement of Long Stability of Sulfur Cathode by Encapsulating Sulfur Into Micropores of Carbon Spheres," *Energy & Environmental Science* 3, no. 10 (2010): 1531–1537, https://doi.org/10.1039/c002639e.

14. Z. Li, L. Yuan, Z. Yi, et al., "Insight Into the Electrode Mechanism in Lithium–Sulfur Batteries With Ordered Microporous Carbon Confined Sulfur as the Cathode," *Advanced Energy Materials* 4, no. 7 (2013): 1301473, https://doi.org/10.1002/aenm.201301473.

15. M. Liu, L. J. Hu, Z. K. Guan, et al., "Tailoring Cathode-Electrolyte Interface for High-Power and Stable Lithium–Sulfur Batteries," *Nano-Micro Letters* 17, no. 1 (2024): 85, https://doi.org/10.1007/s40820-024-01573-4.

16. I. Sungjemmenla, V. S. K., C. B. Soni, V. Kumar, and Z. W. Seh, "Understanding the Cathode–Electrolyte Interphase in Lithium-Ion Batteries," *Energy Technology* 10, no. 9 (2022): 2200421, https://doi.org/10.1002/ente.202200421.

17. J. Gao, M. A. Lowe, Y. Kiya, and H. D. Abruña, "Effects of Liquid Electrolytes on the Charge–Discharge Performance of Rechargeable Lithium/Sulfur Batteries: Electrochemical and In-Situ X-Ray Absorption Spectroscopic Studies," *Journal of Physical Chemistry C* 115, no. 50 (2011): 25132–25137, https://doi.org/10.1021/jp207714c.

18. F. He, X. Wu, J. Qian, et al., "Building a Cycle-Stable Sulphur Cathode by Tailoring Its Redox Reaction Into a Solid-Phase Conversion Mechanism," *Journal of Materials Chemistry A* 6, no. 46 (2018): 23396–23407, https://doi.org/10.1039/c8ta08159j.

19. T. Yim, M.-S. Park, J.-S. Yu, et al., "Effect of Chemical Reactivity of Polysulfide Toward Carbonate-Based Electrolyte on the Electrochemical Performance of Li–S Batteries," *Electrochimica Acta* 107 (2013): 454–460, https://doi.org/10.1016/j.electacta.2013.06.039.

20. Z. Shen, W. Zhang, S. Mao, S. Li, X. Wang, and Y. Lu, "Tailored Electrolytes Enabling Practical Lithium–Sulfur Full Batteries via Interfacial Protection," *ACS Energy Letters* 6, no. 8 (2021): 2673–2681, https://doi.org/10.1021/acsenergylett.1c01091.

21. J. T. Lee, K. Eom, F. Wu, et al., "Enhancing the Stability of Sulfur Cathodes in Li–S Cells via In Situ Formation of a Solid Electrolyte Layer," *ACS Energy Letters* 1, no. 2 (2016): 373–379, https://doi.org/10.1021/acsenergylett.6b00163.

22. F. Huang, L. Gao, Y. Zou, et al., "Akin Solid–Solid Biphasic Conversion of a Li–S Battery Achieved by Coordinated Carbonate Electrolytes," *Journal of Materials Chemistry A* 7, no. 20 (2019): 12498–12506, https://doi.org/10.1039/c9ta02877c.

23. C. Li, Y. Li, Y. Fan, et al., "Mapping Techniques for the Design of Lithium-Sulfur Batteries," *Small* 18, no. 14 (2022): e2106657, https://doi.org/10.1002/smll.202106657.

24. G. Yang, R. Tao, C. J. Jafta, et al., "Investigating Multiscale Spatial Distribution of Sulfur in a CNT Scaffold and Its Impact on Li–S Cell Performance," *Journal of Physical Chemistry C* 125, no. 24 (2021): 13146–13157, https://doi.org/10.1021/acs.jpcc.1c02288.

25. G. Zhou, D.-W. Wang, F. Li, et al., "A Flexible Nanostructured Sulphur–Carbon Nanotube Cathode With High Rate Performance for Li-S Batteries," *Energy & Environmental Science* 5, no. 10 (2012): 8901–8906, https://doi.org/10.1039/c2ee22294a.

26. J. Zhang, Z. Dong, X. Wang, et al., "Sulfur Nanocrystals Anchored Graphene Composite With Highly Improved Electrochemical Performance for Lithium–Sulfur Batteries," *Journal of Power Sources* 270 (2014): 1–8, https://doi.org/10.1016/j.jpowsour.2014.07.089.

27. G. Hu, Z. Sun, C. Shi, et al., "A Sulfur-Rich Copolymer@Cnt Hybrid Cathode With Dual-Confinement of Polysulfides for High-Performance Lithium–Sulfur Batteries," *Advanced Materials* 29, no. 11 (2016): 1603835, https://doi.org/10.1002/adma.201603835.

28. A. Senol Gungor, J. M. von Mentlen, J. G. A. Ruthes, et al., "Understanding Rate and Capacity Limitations in Li-S Batteries Based on Solid-State Sulfur Conversion in Confinement," *ACS Applied Materials & Interfaces* 16, no. 49 (2024): 67651–67661, https://doi.org/10.1021/acsami.4c13183.

29. F. J. García-Soriano, F. Cometto, S. Raviolo, et al., "Biocarbon From Olive Pomace Residue as a Sulfur Host for Carbonate-Based Lithium-Sulfur Batteries," *Communications Materials* 6, no. 1 (2025): 122, https://doi.org/10.1038/s43246-025-00846-8.

30. S. Haber and M. Leskes, "What Can We Learn From Solid State NMR on the Electrode-Electrolyte Interface?," *Advanced Materials* 30, no. 41 (2018): e1706496, https://doi.org/10.1002/adma.201706496.

31. Y. Chen, Q. He, Y. Mo, et al., "Engineering an Insoluble Cathode Electrolyte Interphase Enabling High Performance NCM811//Graphite Pouch Cell at 60°C," *Advanced Energy Materials* 12, no. 33 (2022): 2201631, https://doi.org/10.1002/aenm.202201631.

32. D. Cheng, B. Lu, G. Raghavendran, M. Zhang, and Y. S. Meng, "Leveraging Cryogenic Electron Microscopy for Advancing Battery Design," *Matter* 5, no. 1 (2022): 26–42, https://doi.org/10.1016/j.matt.2021.11.019.

33. K. Liang, X. Yuan, X. Chen, et al., "A Beginner's Guide to Cryo-Em for Battery Research," *Nano Letters* 25, no. 18 (2025): 7210–7223, https://doi.org/10.1021/acs.nanolett.5c00740.

34. X. C. Ren, X. Q. Zhang, R. Xu, J. Q. Huang, and Q. Zhang, "Analyzing Energy Materials by Cryogenic Electron Microscopy," *Advanced Materials* 32, no. 24 (2020): e1908293, https://doi.org/10.1002/adma.201908293.

35. Z. Zhang, J. Yang, W. Huang, et al., "Cathode-Electrolyte Interphase in Lithium Batteries Revealed by Cryogenic Electron Microscopy," *Matter* 4, no. 1 (2021): 302–312, https://doi.org/10.1016/j.matt.2020.10.021.

36. X. Xing, Y. Li, X. Wang, V. Petrova, H. Liu, and P. Liu, "Cathode Electrolyte Interface Enabling Stable Li–S Batteries," *Energy Storage Materials* 21 (2019): 474–480, https://doi.org/10.1016/j.ensm.2019.06.022.

37. W. Huang, D. T. Boyle, Y. Li, et al., "Nanostructural and Electrochemical Evolution of the Solid-Electrolyte Interphase on Cuo Nanowires Revealed by Cryogenic-Electron Microscopy and Impedance Spectroscopy," *ACS Nano* 13, no. 1 (2019): 737–744, https://doi.org/10.1021/acsnano.8b08012.

38. B. Han, Z. Zhang, Y. Zou, et al., "Poor Stability of Li_2Co_3 in the Solid Electrolyte Interphase of a Lithium-Metal Anode Revealed by Cryo-Electron Microscopy," *Advanced Materials* 33, no. 22 (2021): e2100404, https://doi.org/10.1002/adma.202100404.

39. M. J. Zachman, Z. Tu, S. Choudhury, L. A. Archer, and L. F. Kourkoutis, "Cryo-Stem Mapping of Solid-Liquid Interfaces and Dendrites in Lithium-Metal Batteries," *Nature* 560, no. 7718 (2018): 345–349, https://doi.org/10.1038/s41586-018-0397-3.

40. W. Huang, H. Wang, D. T. Boyle, Y. Li, and Y. Cui, "Resolving Nanoscopic and Mesoscopic Heterogeneity of Fluorinated Species in Battery Solid-Electrolyte Interphases by Cryogenic Electron Microscopy," *ACS Energy Letters* 5, no. 4 (2020): 1128–1135, https://doi.org/10.1021/acsenergylett.0c00194.

41. Y. Li, Y. Li, A. Pei, et al., "Atomic Structure of Sensitive Battery Materials and Interfaces Revealed by Cryo–Electron Microscopy," *Science* 358, no. 6362 (2017): 506–510.

42. C. X. Bi, N. Yao, X. Y. Li, et al., "Unveiling the Reaction Mystery Between Lithium Polysulfides and Lithium Metal Anode in Lithium-Sulfur Batteries," *Advanced Materials* 36, no. 41 (2024): e2411197, https://doi.org/10.1002/adma.202411197.

43. X. Wang, Y. Li, and Y. S. Meng, "Cryogenic Electron Microscopy for Characterizing and Diagnosing Batteries," *Joule* 2, no. 11 (2018): 2225–2234, https://doi.org/10.1016/j.joule.2018.10.005.

44. J. Conder, C. Marino, P. Novák, and C. Villevieille, "Do Imaging Techniques Add Real Value to the Development of Better Post-Li-Ion Batteries?," *Journal of Materials Chemistry A* 6, no. 8 (2018): 3304–3327, https://doi.org/10.1039/c7ta10622j.

45. S. Zhou, J. Shi, S. Liu, et al., "Visualizing Interfacial Collective Reaction Behaviour of Li-S Batteries," *Nature* 621, no. 7977 (2023): 75–81, https://doi.org/10.1038/s41586-023-06326-8.

46. Z. Ju, H. Yuan, O. Sheng, et al., "Cryo-Electron Microscopy for Unveiling the Sensitive Battery Materials," *Small Science* 1, no. 11 (2021): 2100055, https://doi.org/10.1002/smsc.202100055.

47. D. B. Nash, "Sulfur in Vacuum: Sublimation Effects on Frozen Melts, and Applications to Io's Surface and Torus," *Icarus* 72 (1987): 1–34.

48. C. Raiß, K. Peppler, J. Janek, and P. Adelhelm, "Pitfalls in the Characterization of Sulfur/Carbon Nanocomposite Materials for Lithium–Sulfur Batteries," *Carbon* 79 (2014): 245–255, https://doi.org/10.1016/j.carbon.2014.07.065.

49. B. D. A. Levin, M. J. Zachman, J. G. Werner, et al., "Characterization of Sulfur and Nanostructured Sulfur Battery Cathodes in Electron Microscopy Without Sublimation Artifacts," *Microscopy and Microanalysis* 23, no. 1 (2017): 155–162, https://doi.org/10.1017/S1431927617000058.

50. K. Liao and A. Manthiram, "Impact of Cathode Microstructure on Sulfur Redox Kinetics in Lithium–Sulfur Batteries," *Advanced Energy Materials* 15 (2025): 2502062, https://doi.org/10.1002/aenm.202502062.

51. Z. X. Chen, Q. Cheng, X. Y. Li, et al., "Cathode Kinetics Evaluation in Lean-Electrolyte Lithium-Sulfur Batteries," *Journal of the American*

Chemical Society 145, no. 30 (2023): 16449–16457, https://doi.org/10.1021/jacs.3c02786.

52. X. Ji and L. F. Nazar, "Advances in Li–S Batteries," *Journal of Materials Chemistry* 20, no. 44 (2010): 9821, https://doi.org/10.1039/b925751a.

53. M. L. Para, C. A. Calderón, S. Drvarič Talian, et al., "Extending the Conversion Rate of Sulfur Infiltrated Into Microporous Carbon in Carbonate Electrolytes," *Batteries & Supercaps* 5, no. 5 (2022): e202100374, https://doi.org/10.1002/batt.202100374.

54. T. Li, X.-Q. Zhang, P. Shi, and Q. Zhang, "Fluorinated Solid-Electrolyte Interphase in High-Voltage Lithium Metal Batteries," *Joule* 3, no. 11 (2019): 2647–2661, https://doi.org/10.1016/j.joule.2019.09.022.

55. J. M. von Mentlen, A. S. Güngör, T. Demuth, et al., "Unraveling Multiphase Conversion Pathways in Lithium-Sulfur Batteries Through Cryo Transmission Electron Microscopy and Machine Learning-Assisted Operando Neutron Scattering," *ACS Nano* 19, no. 17 (2025): 16626–16638, https://doi.org/10.1021/acsnano.5c00536.

56. X. Q. Zhang, T. Li, B. Q. Li, et al., "A Sustainable Solid Electrolyte Interphase for High-Energy-Density Lithium Metal Batteries Under Practical Conditions," *Angewandte Chemie International Edition* 59, no. 8 (2020): 3252–3257, https://doi.org/10.1002/anie.201911724.

57. A. Vizintin, M. Lozinšek, R. K. Chellappan, et al., "Fluorinated Reduced Graphene Oxide as an Interlayer in Li–S Batteries," *Chemistry of Materials* 27, no. 20 (2015): 7070–7081, https://doi.org/10.1021/acs.chemmater.5b02906.

58. D. J. Tarimo, F. J. García-Soriano, A. Vizintin, C. Prehal, and V. Presser, "Performance of Microporous Carbon Cathodes and Impact of Cathode/Solid Electrolyte Interphase Formation Using Carbonate and Ether-Based Electrolytes in Lithium–Sulfur Batteries," *ACS Applied Energy Materials* 8, no. 16 (2025): 12139–12156, https://doi.org/10.1021/acsaem.5c01629.

59. Y. Zhong, K. R. Yang, W. Liu, P. He, V. Batista, and H. Wang, "Mechanistic Insights Into Surface Chemical Interactions Between Lithium Polysulfides and Transition Metal Oxides," *Journal of Physical Chemistry C* 121, no. 26 (2017): 14222–14227, https://doi.org/10.1021/acs.jpcc.7b04170.

60. F. J. García-Soriano, S. A. Ceppi, F. P. Cometto, et al., "Sepiolite as a Novel Polysulfide Trapper for Energy Applications: An Electrochemical, X-Ray Spectroscopic and DFT Study," *Physical Chemistry Chemical Physics* 25, no. 36 (2023): 24761–24769, https://doi.org/10.1039/d3cp03157h.

61. Y. Wang, Y. Liu, Y. Tu, and Q. Wang, "Reductive Decomposition of Solvents and Additives Toward Solid-Electrolyte Interphase Formation in Lithium-Ion Battery," *Journal of Physical Chemistry C* 124, no. 17 (2020): 9099–9108, https://doi.org/10.1021/acs.jpcc.9b10535.

62. C. Xu, F. Lindgren, B. Philippe, et al., "Improved Performance of the Silicon Anode for Li-Ion Batteries: Understanding the Surface Modification Mechanism of Fluoroethylene Carbonate as an Effective Electrolyte Additive," *Chemistry of Materials* 27, no. 7 (2015): 2591–2599, https://doi.org/10.1021/acs.chemmater.5b00339.

63. H. Kim, F. Wu, J. T. Lee, et al., "In Situ Formation of Protective Coatings on Sulfur Cathodes in Lithium Batteries With Lifsi-Based Organic Electrolytes," *Advanced Energy Materials* 5, no. 6 (2014): 1401792, https://doi.org/10.1002/aenm.201401792.

64. J. Tan, J. Matz, P. Dong, J. Shen, and M. Ye, "A Growing Appreciation for the Role of Lif in the Solid Electrolyte Interphase," *Advanced Energy Materials* 11, no. 16 (2021): 2100046, https://doi.org/10.1002/aenm.202100046.

65. S. Lorger, K. Narita, R. Usiskin, and J. Maier, "Enhanced Ion Transport in Li_2O and Li_2S Films," *Chemical Communications* 57, no. 53 (2021): 6503–6506, https://doi.org/10.1039/d1cc00557j.

66. D. Wang, B. Gwalani, D. Wierzbicki, et al., "Overcoming the Conversion Reaction Limitation at Three-Phase Interfaces Using Mixed Conductors Towards Energy-Dense Solid-State Li-S Batteries," *Nature Materials* 24, no. 2 (2025): 243–251, https://doi.org/10.1038/s41563-024-02057-x.

67. C. Wang, K. Adair, and X. Sun, "All-Solid-State Lithium Metal Batteries With Sulfide Electrolytes: Understanding Interfacial Ion and Electron Transport," *Accounts of Materials Research* 3, no. 1 (2021): 21–32, https://doi.org/10.1021/accountsmr.1c00137.

68. X. Zhu, L. Wang, Z. Bai, J. Lu, and T. Wu, "Sulfide-Based All-Solid-State Lithium-Sulfur Batteries: Challenges and Perspectives," *Nano-Micro Letters* 15, no. 1 (2023): 75, https://doi.org/10.1007/s40820-023-01053-1.

69. F. Y. Fan, W. C. Carter, and Y. M. Chiang, "Mechanism and Kinetics of Li_2S Precipitation in Lithium-Sulfur Batteries," *Advanced Materials* 27, no. 35 (2015): 5203–5209, https://doi.org/10.1002/adma.201501559.

70. H. Yuan, H. J. Peng, J. Q. Huang, and Q. Zhang, "Sulfur Redox Reactions at Working Interfaces in Lithium–Sulfur Batteries: A Perspective," *Advanced Materials Interfaces* 6, no. 4 (2019): 1802046, https://doi.org/10.1002/admi.201802046.

71. Y. Shin, D. Stepien, M. Hepp, B. Butz, D. Bresser, and S. Fleischmann, "Cryogenic Electron Microscopy Workflows for the Characterization of Electrochemical Interfaces and Interphases in Batteries," *Journal of Power Sources* 556 (2023): 232515, https://doi.org/10.1016/j.jpowsour.2022.232515.

Supporting Information

Additional supporting information can be found online in the Supporting Information section.

Figure S1: Raman spectra of AC08 powders prepared with different ball milling speeds. **Figure S2:** TGA results of AC08 powders with prepared with different ball milling speeds. **Figure S3:** Long term cycling performance of electrodes prepared at different ball milling speeds with a mass ratio of 1:1. **Figure S4:** Normalized relaxation curves of electrodes prepared at different ball milling speeds (mass ratio 1:1), recorded at OCV during GITT. **Figure S5:** Reference EELS spectra based on Gatan EELS Atlas. **Figure S6:** Transmission electron microscopy (TEM) measurements for 800-rpm ball milled particles after the first discharge. **Figure S7:** Scanning electron micrographs of electrodes after the first discharge: (a) non-ball milled (b) 500-rpm ball milled and (c) 800-rpm ball milled. **Figure S8:** Representative spherical masks used for particle size distribution analysis. **Table S1:** Detailed XPS data representing elemental content in atomic percent. **Table S2:** Type of function, binding energies (BE), full width half maxima (FWHM), and source of the C 1*s* deconvoluted spectra in Figure 4. **Table S3:** Type of function, binding energies (BE), full width half maxima (FWHM) and source of the F 1*s* deconvoluted spectra in Figure 4. **Table S4:** Type of function, binding energies (BE), full width half maxima (FWHM) and source of the P 1*p* deconvoluted spectra in Figure 4. **Table S5:** Type of function, binding energies (BE), full width half maxima (FWHM) and source of the S 2*p* deconvoluted spectra in Figure 4. **Table S6:** Type of function, binding energies (BE), full width half maxima (FWHM) and source of the Li 1*s* deconvoluted spectra in Figure 4.